ELSEVIER

Journal of Fluids and Structures 22 (2006) 599–615

JOURNAL OF FLUIDS AND STRUCTURES

www.elsevier.com/locate/jfs

Optical fiber instability during coating process

M. Hamadiche[a,*], H. Abou-Shady[b]

[a]*Laboratoire de Mécanique des Fluides et d'Acoustique, École Centrale de Lyon, 36 Av. Guy de Collongue, UMR5509 F 69134 Ecully, France*

[b]*Department of Physics, Faculty of Science, Cairo University, Egypt*

Received 10 June 2004; accepted 25 February 2006
Available online 2 May 2006

Abstract

In the present work, we study the stability of a system designed for the coating of optical fiber. This is achieved by studying the stability of the flowing resin in the die while coupled with a viscoelastic optical fiber. We develop a numerical code based on a sixth-order compact finite-difference method in order to solve the two-dimensional Navier–Stokes equations. We show that there is a bifurcation flow for a given value of the Reynolds number, wherever the vibration of the optical fiber has been experimentally observed. The stability of the resulting flow, coupled with a nonrigid optical fiber, is considered. Two-dimensional and three-dimensional stability analyses were made. The system was found to be subjected to two kinds of instability induced by two distinguishable groups of modes. For an optical fiber with a small radius, we assume that the preceding vibration may not be the only cause of the irregularity in the coating thickness. Therefore, a model taking into account the deformation of the liquid resin surface, under the action of the surface-tension forces, before resin solidification, and after leaving the die, is proposed. This model assumes that the liquid layer is subjected to surface-tension and gravity forces. It was found that the dynamic equation depends on two dimensionless parameters. It is found that the surface of the fiber has a wavy form. The length of the wave depends on the two dimensionless parameters. Our work shows qualitative agreement with the experimental results without adjusting arbitrary constants.

1. Introduction

The aim of this work is to study the stability of the optical-fiber coating system. The use of optical fibers is increasing, thus manufacturers need to increase its production. An increase in the production could be achieved by faster manufacturing processes. As far as the coating system is concerned, this requires a high traveling speed of the optical fiber across the liquid resin, during the coating process. However, the optical fiber's speed is limited by the instability of the system, which may induce a vibration harming the coating quality. Our objective in this paper is to find the origin of this instability by analyzing the stability of the coating system. The coating system depicted in Fig. 1, shows an optic fiber traveling at speed V_f over some rollers and passing through a resin-filled die. The die, a component of the system, is depicted more clearly in Fig. 2. The die is supplied laterally by the resin while it is dragged by the optical fiber, which forms a coat after it leaves the die. The die ends by a small hollow cylinder in order to keep the flow uniform and

*Corresponding author. Tel.: +33 472186167; fax: +33 478647145.
E-mail address: mahmoud.hamadiche@ec-lyon.fr (M. Hamadiche).

0889-9746/$ - see front matter © 2006 Elsevier Ltd. All rights reserved.
doi:10.1016/j.jfluidstructs.2006.02.005

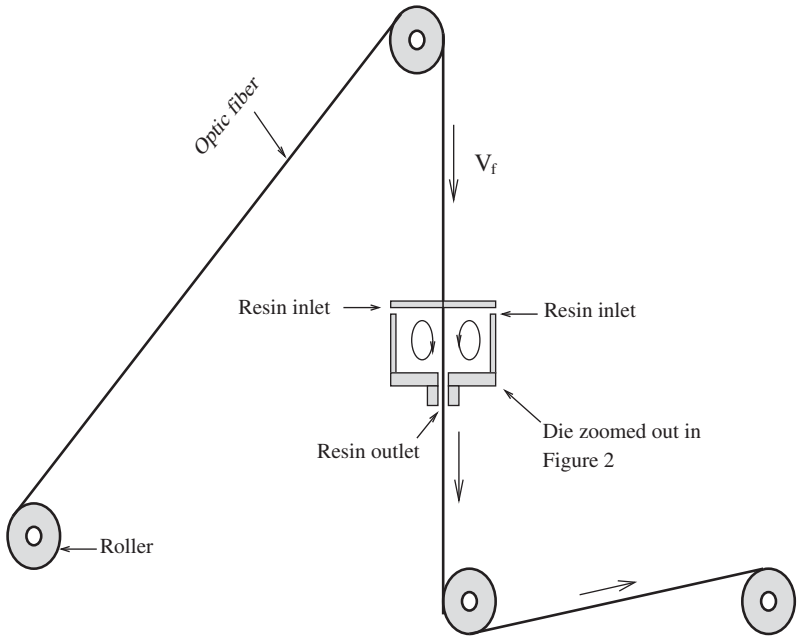

Fig. 1. A sketch of the coating system.

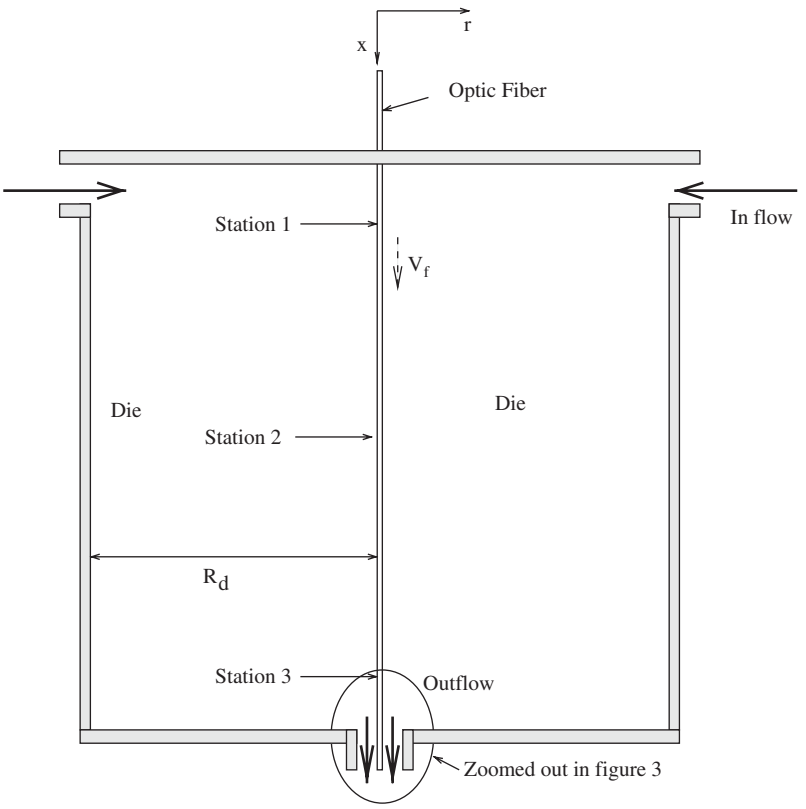

Fig. 2. A sketch of the die.

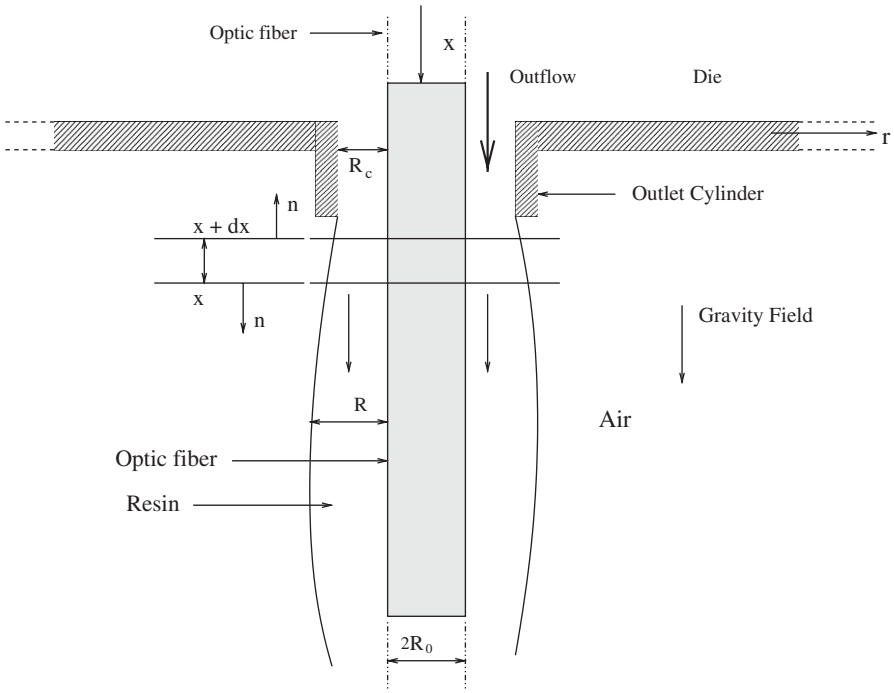

Fig. 3. Sketch of the outlet of the die.

parallel to the axis of the optical fiber, at the outlet of the die. The outlet of the die which includes the hollow small cylinder, is zoomed out in Fig. 3.

The dimensions of the microdevices used during the flow influences the model. When the microdevices are large enough, the fluid is considered a continuum medium. In the present work, we assume that the radius of the optical fiber, as well as the die dimensions, are large enough to consider the fluid as a continuum medium. The results are less accurate for extremely small radii of optical fibers and very small dies. The limit of validity of the continuum model is discussed thoroughly by Gad-el-Hak (1999). In this work, the fluid is assumed to satisfy the incompressible Navier–Stokes equations.

The sixth-order compact finite-difference schemes,[1] implemented by an alternating-direction implicit procedure, using the Thomas algorithm, is used to solve the two-dimensional Navier–Stokes equations in the (ψ, ω) formulation; at this stage the optical fiber is assumed to be rigid and traveling at constant speed. The stability of the coating system, in the vicinity of the obtained dynamic equilibrium position will be studied, when the basic flow is obtained. In these studies, the optical fiber is considered as a viscoelastic medium. The disturbance in the optical fiber and the in-flow within the die are coupled via the boundary conditions. Both axisymmetric and nonaxisymmetric disturbances are considered.

Section 2 will recall the two-dimensional Navier–Stokes equations in (ψ, ω) formulation and the boundary conditions describing the flow in the die. In Section 3, the method used to solve the Navier–Stokes equations is described. In Section 4, we interpret the obtained steady solution. In Section 5, we study the stability of the dynamic equilibrium steady state when subjected to an infinitesimal disturbance. The optical fiber is considered as a viscoelastic material interacting with the flow in the die. The analysis will be carried out by considering an infinitesimal disturbance in the form of a normal mode. In Section 6, a numerical approach is developed to find the eigenvalues of the system and to view its stability. In Sections 8 and 9, the temporal eigenvalues of the system will be discussed. A model tackling the deformation of the coating surface by the surface-tension and gravity forces is developed in Section 10. A conclusion is provided in Section 11.

[1]The compact finite-difference schemes is an implicit finite-difference method. The difference equation involves the function as well as its derivatives, which increases the precision of the schemes without an increase in the number of the grid points involved in the computation. See Hirsch (1997, vol. 1).

1.1. Previous experimental work and models

The stability of the coating system has been studied experimentally by Kaneko et al. (2002). In their experiment, an optical fiber is drawn from a bobbin to a top roller that passes through a die of tapered form, filled up by a resin. When the optical fiber leaves the die, it is subjected to UV light to dry it, before leading it to a second bobbin. The die in this experiment has a tapered form and ends by a straight section of cylindrical form. The die is supplied by the resin through its large section. The flow at the inlet of the die is perpendicular to the axes of the fiber. The experimental results show that the system is stable if the speed of the optical fiber does not exceed some critical value, determined by the experiment. For velocities higher than the threshold (about 1000 m/min), the system becomes unstable. The critical Reynolds number, based on the width of annular outlet passage, d_c, and the speed of the optical fiber, is found to be in the range, $0.2 < \tilde{\mathrm{Re}}_c < 1.2$.

1.2. Prior theoretical studies

A theoretical model has been proposed by Kaneko et al. (2002), in order to understand the origin of this instability. The work neglected the analysis of the flow within the die. It added difficulty to the theoretical calculation. Moreover, only the interaction between the flow in the small cylindrical outlet tube and the optical fiber is considered in their model. Their theoretical model has a disadvantage in the form of two tailored arbitrary constants. These constants are included to obtain a qualitative agreement between experimental and theoretical results, without a theoretical foundation.

In their model, Kaneko et al. (2002) assume that the instability is due to the interaction between the optical fiber, seen as an elastic solid, and the flow in the straight cylindrical section at the outlet of the die. The gap between the cylindrical rigid wall and the surface of the optical fiber is considered small enough to neglect the curvature of the wall. The mathematical model proposed by Inada and Hayama (1990a, b) has been used in order to model the flow. The flow equations are solved numerically and the unsteady pressure is computed. They predict the motion of the optical fiber with the unsteady pressure at its surface. In their approach, the moving-string model proposed by Tajima (1970) is used to describe the motion of the optical fiber far from the die. In the die outlet, where the interaction between the flow and the optical fiber is supposed to take place, the model involves a kinematic assumption about the motion of the optical fiber. We refer to their paper for more information. Our insight is that the vibration of the optical fiber is due to the instability of the flow in the die, interacting with the optical fiber that can be considered as a viscoelastic medium.

2. Basic flow formulation

We consider a two-dimensional flow within the die that satisfies the two-dimensional Navier–Stokes equations. We opt for a (ψ, ω) formulation; ψ and ω represent the stream function and the vorticity, respectively. The advantage of this formulation lies in the fact that it does not contain the pressure term in the Navier–Stokes equations and has a reduced number of dependent variables. Let ψ and ω be defined such that

$$v_r = -\frac{1}{r}\frac{\partial \psi}{\partial x}, \quad v_x = \frac{1}{r}\frac{\partial \psi}{\partial r}, \quad \omega = \frac{\partial v_r}{\partial x} - \frac{\partial v_x}{\partial r};$$

ω and ψ obey the following equations (Batchelor, 1967):

$$\frac{\partial^2 \psi}{\partial x^2} + \frac{\partial^2 \psi}{\partial r^2} - \frac{1}{r}\frac{\partial \psi}{\partial r} = -r\omega, \tag{1}$$

$$\frac{\partial \omega}{\partial t} + v_x \frac{\partial \omega}{\partial x} + v_r \frac{\partial \omega}{\partial r} - \frac{v_r}{r}\omega = \frac{1}{\mathrm{Re}}\left(\frac{\partial^2 \omega}{\partial r^2} + \frac{1}{r}\frac{\partial \omega}{\partial r} + \frac{\partial^2 \omega}{\partial x^2} - \frac{\omega}{r^2}\right). \tag{2}$$

In these equations, the velocity is scaled by the speed V_f of the optical fiber, the distance by the radius R_d of the die and the time by $R_d V_f^{-1}$. The Reynolds number is $\mathrm{Re} = V_f R_d / \nu$, where ν is the kinematic viscosity of the resin. Let R_c be the gap between the small cylinder at the outlet of the die and the surface of optical fiber; we define another Reynolds number $\tilde{\mathrm{Re}}$ based on R_c, such that $\tilde{\mathrm{Re}} = V_f R_c / \nu$; therefore, $\tilde{\mathrm{Re}} = R_c\,\mathrm{Re}/R_d$. The previous equations are associated with the following boundary conditions:

(i) $\psi = 0$ at the upper part of the wall of the die and at the optical fiber, shown in Fig. 2;
(ii) ψ varies linearly with x at the inlet of the die shown in Fig. 2 and $\partial\psi/\partial n = 0$ at the outlet of the die shown in the same figure, n being normal to the outlet section;

(iii) $\psi = \psi_d = 0.001$, on the lower part of the die wall shown in Fig. 2;
(iv) the no-slip condition, as well as the continuity equation, are used to connect ω to ψ, at the wall.

3. Numerical method for the basic flow

The discretization of time allows the transformation of the previous nonlinear equations to a system of second-order differential equations in x or r direction. The previous nonlinear equations are solved by the compact sixth-order finite-difference method, implemented by the Thomas algorithm. The iteration in time is pursued until a steady solution is obtained. The direction r and x are alternated at each time step [ADI method; see Hirsch (1997)]. In order to verify the accuracy of our algorithm, we check its core by solving some differential equations of known solution and comparing our numerical results with the exact known solution. The error was less than one per cent for 13 points in the range $(0, 1)$. The whole code is used to solve the cavity problem and the two-dimensional flow in a divergent channel flow. The obtained results are compared to the known results [see Al-Farkh (1998)].

4. Basic flow description

A series of numerical tests have been performed for some Reynolds number values around the experimental critical value. The die considered, is such that $0.1 \leqslant r \leqslant 1$ and $-2 \leqslant x \leqslant 2$. Knowing that the vibration of the optical fiber observed by the experiment has a Reynolds number $\tilde{\mathrm{Re}}$ in the range $(0.2, 1.2)$, the numerical experiment has been performed for some values of Reynolds number $\tilde{\mathrm{Re}}$, in the range $(0.01, 100)$. It was found that the flow in the die was a single-cell pattern if the Reynolds number is less than 0.2 and a two-cell patterns if the Reynolds number exceeds 1 (see Fig. 4). Only two-cell patterns have been observed when the Reynolds number varies in the range (1, 100). However, the form of the pattern changes with increasing Reynolds number. Fig. 5 shows the velocity profiles in three stations as a function of the distance from the optical fiber. The stations are localized at $x = -1.34$, 0, and 1.34. Fig. 5(a) shows the axial velocity for $\tilde{\mathrm{Re}} = 5$. As one can see, this profile has an inflection point and therefore has to be subjected to inviscid flow instabilities. Fig. 5(b) shows that the axial velocity profile for $\tilde{\mathrm{Re}} = 0.1$ has no such inflexion point. Figs. 5(c) and (d) show that the velocity profile has a large gradient near the optical fiber for both Reynolds number values. It is found that the axial derivative of the velocity field of the basic flow is small with respect to the radial derivative. This allows us to perform a local stability analysis, by neglecting the variation of the flow, in the axial direction. Therefore, the validity of this analysis will be limited to waves that are short in comparison with the length of the die.

5. Basic flow stability

Our task is to study the stability of an incompressible Newtonian fluid of density ρ and dynamic viscosity η, flowing in a die, around a viscoelastic optical fiber translating at speed V_f. The viscoelastic optical fiber is made of an incompressible, viscoelastic material of density ρ equal to the fluid density, viscosity η_s, and shear modulus G (shown in Fig. 2). In this paper, we use dimensionless variables. The length scale is the radius of the die R_d, the time scale is $(\rho R_d^2/G)^{1/2}$, and the velocity scale is $(G/\rho)^{1/2}$. The dimensionless mean flow velocity profile in cylindrical coordinates is obtained numerically in the preceding section:

$$\vec{V} = \Gamma(U_x, U_r, 0), \tag{3}$$

where $\Gamma = (\rho V_f^2/G)^{1/2}$. The governing equations for the fluid are the continuity and momentum equations

$$\partial_i v_i = 0, \tag{4}$$

$$\partial_t v_i + v_j \partial_j v_i = -\partial_i p + \varepsilon \Gamma \partial_j^2 v_i, \tag{5}$$

where $\partial_t = \partial/\partial t$, $\partial_j = \partial/\partial x_j$, $\varepsilon = \mathrm{Re}^{-1}$, and $\mathrm{Re} \equiv \rho V_f R_d/\eta$ is the Reynolds number as defined before. The pressure, p, in the fluid is nondimensionalized by the shear modulus G. The optical fiber is modeled using the dynamical equations for an incompressible viscoelastic material (Landau and Lifshitz, 1970). The dynamics of the optical fiber is described by a displacement field u_i, which represents the displacement of material points from their steady-state positions, under the action of the stresses at the interface. For an incompressible material, the displacement field u_i satisfies the

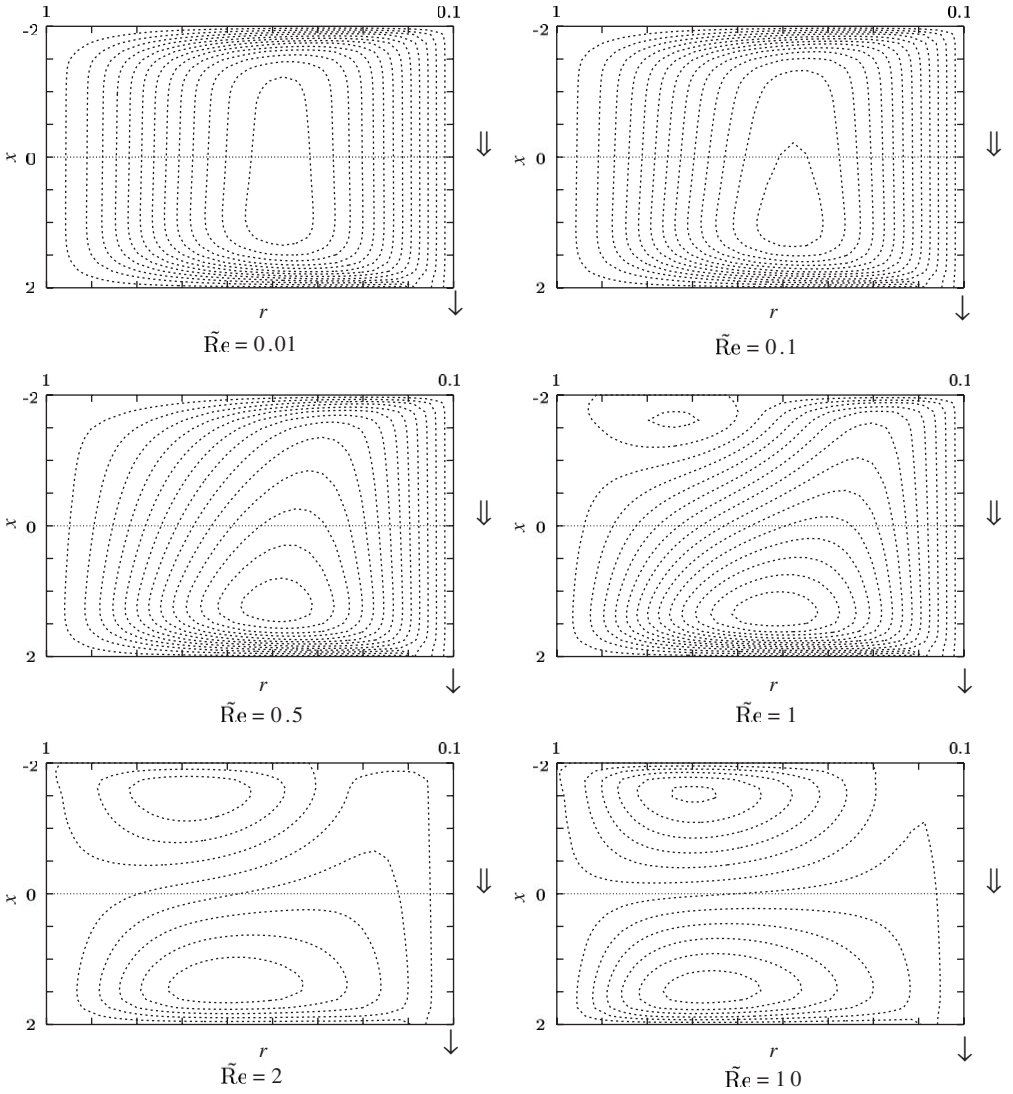

Fig. 4. The streamlines in the (x, r)-plane for several Reynolds number values.

solenoidal condition

$$\partial_i u_i = 0, \tag{6}$$

and the momentum conservation equation is

$$\partial_t^2 u_i = -\partial_i p + \partial_j^2 u_i + \varepsilon \Gamma \eta_r \partial_j^2 v_i. \tag{7}$$

The left-hand side represents the rate of change of momentum per unit volume. The three terms on the right-hand side are, respectively, the pressure gradient, the divergence of the elastic stress due to the strain in the material, and the divergence of the viscous stress due to the strain rate. Lastly, the wall velocity is given by $v_i = \partial_t u_i$, and $\eta_r = \eta_s/\eta$.

5.1. Nonaxisymmetric disturbances

In the linear stability analysis, small perturbations in the form of Fourier modes are introduced in the fluid velocity field and the wall displacement field

$$(v_j, p) = (\widetilde{v}_j, \widetilde{p}) \mathrm{e}^{(\mathrm{i}kx + \mathrm{i}n\theta + st)} + cc, \tag{8}$$

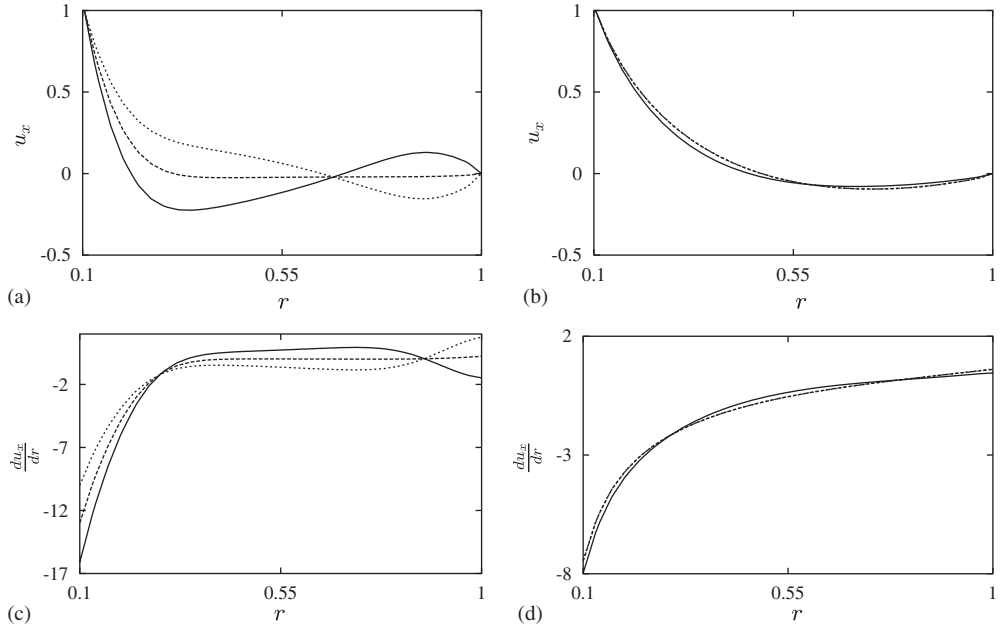

Fig. 5. (a) and (b) The axial velocity as function of the radial distance at three stations: —, $x = -1.34$; - - -, $x = 0$; ....., $x = 2.34$; (a) $\tilde{\mathrm{Re}} = 5$, (b) $\tilde{\mathrm{Re}} = 0.1$. (c) and (d) The derivative with respect to r of the axial velocity as function of the radial distance at the three stations: —, $x = -1.34$; - - -, $x = 0$; ...., $x = 2.34$; (c) $\tilde{\mathrm{Re}} = 5$, (d) $\tilde{\mathrm{Re}} = 0.1$.

$$(u_j, p) = (\widetilde{u_j}, \widetilde{p})\mathrm{e}^{(\mathrm{i}kx + \mathrm{i}n\theta + st)} + cc, \tag{9}$$

where $\widetilde{v_j}$ and $\widetilde{u_j}$ are the eigenfunctions which are functions of r only, k and n are the axial and the Azimuthal wave numbers, respectively, p is the pressure disturbance, and cc stands for complex conjugate. The real part of the eigenvalue s is the (temporal) growth rate of the perturbation, and the imaginary part is the frequency. Upon inserting the above perturbation velocity into the conservation equations for the fluid velocity field (4) and (5), and neglecting the nonlinear terms in $\widetilde{v_j}$ and the terms involving the x-wise derivation of the basic flow, the following equations are obtained for the eigenfunction $\widetilde{v_j}$ in cylindrical coordinates:

$$[d_r + r^{-1}]\widetilde{v_r} + \mathrm{i}k\widetilde{v_x} + \mathrm{i}nr^{-1}\widetilde{v_\theta} = 0, \tag{10}$$

$$[s + \mathrm{i}k\Gamma U_x]\widetilde{v_r} + U_r d_r\widetilde{v_r} + \widetilde{v_r} d_r U_r = -d_r\widetilde{p} + \varepsilon\Gamma\{[d_r^2 + r^{-1}d_r - r^{-2}(1+n^2) - k^2]\widetilde{v_r} - 2\mathrm{i}nr^{-2}\widetilde{v_\theta}\}, \tag{11}$$

$$[s + \mathrm{i}k\Gamma U_x]\widetilde{v_x} + d_r U_x\widetilde{v_r} + U_r d_r\widetilde{v_x} = -\mathrm{i}k\widetilde{p} + \varepsilon\Gamma[d_r^2 + r^{-1}d_r - (k^2 + n^2r^{-2})]\widetilde{v_x}, \tag{12}$$

$$[s + \mathrm{i}k\Gamma U_x]\widetilde{v_\theta} + U_r d_r\widetilde{v_\theta} = -\mathrm{i}n\widetilde{p}r^{-1} + \varepsilon\Gamma\{[d_r^2 + r^{-1}d_r - r^{-2}(1+n^2) - k^2]\widetilde{v_\theta} + 2\mathrm{i}nr^{-2}\widetilde{v_r}\}, \tag{13}$$

where d_r stands for derivative with respect to r, and $\widetilde{p}(r)$ is the eigenfunction for the pressure. Similarly, the equations for the eigenfunction $\widetilde{u_j}$ could be obtained by inserting Eq. (9) for the solid displacement perturbation into the conservation equations (6) and (7), yielding in cylindrical coordinates

$$[d_r + r^{-1}]\widetilde{u_r} + \mathrm{i}k\widetilde{u_x} + \mathrm{i}nr^{-1}\widetilde{u_\theta} = 0, \tag{14}$$

$$s^2\widetilde{u_r} = -d_r\widetilde{p} + (1 + \varepsilon\Gamma\eta_r s)\{[d_r^2 + r^{-1}d_r - r^{-2}(1+n^2) - k^2]\widetilde{u_r} - 2\mathrm{i}nr^{-2}\widetilde{u_\theta}\}, \tag{15}$$

$$s^2\widetilde{u_x} = -\mathrm{i}k\widetilde{p} + (1 + \varepsilon\Gamma\eta_r s)[d_r^2 + r^{-1}d_r - (k^2 + n^2r^{-2})]\widetilde{u_x}, \tag{16}$$

$$s^2\widetilde{u_\theta} = -\mathrm{i}nr^{-1}\widetilde{p} + (1 + \varepsilon\Gamma\eta_r s)\{[d_r^2 + r^{-1}d_r - r^{-2}(1+n^2) - k^2]\widetilde{u_\theta} + 2\mathrm{i}nr^{-2}\widetilde{u_r}\}. \tag{17}$$

The boundary conditions at the center of the optical fiber $r = 0$, when applied to the azimuthally varying modes with Azimuthal wavenumber $n = 1$, are

$$\widetilde{u_r} + \mathrm{i}\widetilde{u_\theta} = 0, \tag{18}$$

$$\widetilde{u}_x = \widetilde{p} = 0. \tag{19}$$

At the interface $r = 0.1$, we enforce the velocity continuity

$$\widetilde{v}_r + d_r U_r \widetilde{u}_r = s\widetilde{u}_r, \tag{20}$$

$$\widetilde{v}_x + d_r U_x \widetilde{u}_r = s\widetilde{u}_x, \tag{21}$$

$$\widetilde{v}_\theta = s\widetilde{u}_\theta, \tag{22}$$

and the continuity of the stress

$$\widetilde{\sigma}_{rr} = \widetilde{\tau}_{rr}, \quad \widetilde{\sigma}_{r\theta} = \widetilde{\tau}_{r\theta}, \quad \widetilde{\sigma}_{rx} = \widetilde{\tau}_{rx} \tag{23}$$

and at the surface $r = 1$, we enforce the no slip condition

$$\widetilde{v}_r = 0, \quad \widetilde{v}_\theta = 0, \quad \widetilde{v}_x = 0. \tag{24}$$

The terms $d_r U_r \widetilde{u}_r$ and $d_r U_x \widetilde{u}_r$ in (20) and (21) represent the variation of the mean velocity at the interface due to the surface displacement. The boundary conditions at $r = 0$, applied to the two components of the nonaxisymmetric eigenmodes $(\widetilde{v}_r, \widetilde{v}_\theta)$ with Azimuthal wave number $n > 1$, are

$$\widetilde{u}_r = \widetilde{u}_\theta = 0, \tag{25}$$

the remaining boundary conditions are identical to those applied to the eigenmodes with Azimuthal wave number $n = 1$.

The linearized mass and momentum equations for the fluid and solid can be transformed to a system of first-order differential equations. In order to do that, we take the derivative with respect to r of all the terms in the continuity Eqs. (10) and (14). This yields

$$\left[d_r^2 + r^{-1}d_r - r^{-2}\right]\widetilde{v}_r + \mathrm{i}k d_r \widetilde{v}_x + \mathrm{i}n d_r(r^{-1}\widetilde{v}_\theta) = 0, \tag{26}$$

$$\left[d_r^2 + r^{-1}d_r - r^{-2}\right]\widetilde{u}_r + \mathrm{i}k d_r \widetilde{u}_x + \mathrm{i}n d_r(r^{-1}\widetilde{u}_\theta) = 0; \tag{27}$$

Eqs. (26) and (27) give $d_r^2\widetilde{v}_r$ and $d_r^2\widetilde{u}_r$ as functions of the velocity and displacement components and their first-order derivatives. If these functions are substituted into (11)–(13) and (15)–(17), the system can be transformed to the following first-order differential equations, for the fluid:

$$d_r \widetilde{v}_r = -r^{-1}v_r - \mathrm{i}k\widetilde{v}_x - \mathrm{i}nr^{-1}\widetilde{v}_\theta, \tag{28}$$

$$d_r \widetilde{p} = -[s + \Gamma \mathrm{i}k(1 - r^2)]\widetilde{v}_r - \varepsilon\Gamma\{(r^{-2}n^2 + k^2)\widetilde{v}_r + \mathrm{i}nr^{-2}\widetilde{v}_\theta + \mathrm{i}k\widetilde{\xi}_x + \mathrm{i}nr^{-1}\widetilde{\xi}_\theta\}, \tag{29}$$

$$d_r \widetilde{\xi}_x = -r^{-1}\widetilde{\xi}_x + (k^2 + n^2r^{-2})\widetilde{v}_x + (\varepsilon\Gamma)^{-1}[s + \Gamma \mathrm{i}k(1 - r^2)]\widetilde{v}_x - 2\varepsilon^{-1}r\widetilde{v}_r + \mathrm{i}k(\varepsilon\Gamma)^{-1}\widetilde{p}, \tag{30}$$

$$d_r \widetilde{v}_x = \widetilde{\xi}_x, \tag{31}$$

$$d_r \widetilde{\xi}_\theta = -r^{-1}\widetilde{\xi}_\theta + [r^{-2}(1 + n^2) + k^2]\widetilde{v}_\theta - 2\mathrm{i}nr^{-2}\widetilde{v}_r + (\varepsilon\Gamma)^{-1}[s + \Gamma \mathrm{i}k(1 - r^2)]\widetilde{v}_\theta + \mathrm{i}n(r\varepsilon\Gamma)^{-1}\widetilde{p}, \tag{32}$$

$$d_r \widetilde{v}_\theta = \widetilde{\xi}_\theta, \tag{33}$$

and the following first-order differential for the compliant solid

$$d_r \widetilde{u}_r = -r^{-1}u_r - \mathrm{i}k\widetilde{u}_x - \mathrm{i}nr^{-1}\widetilde{u}_\theta, \tag{34}$$

$$d_r \widetilde{p} = -s^2\widetilde{u}_r - (1 + \varepsilon\Gamma\eta_r s)\{(r^{-2}n^2 + k^2)\widetilde{u}_r + \mathrm{i}nr^{-2}\widetilde{u}_\theta + \mathrm{i}k\widetilde{\chi}_x + \mathrm{i}nr^{-1}\widetilde{\chi}_\theta\}, \tag{35}$$

$$d_r \widetilde{\chi}_x = -r^{-1}\widetilde{\chi}_x + (k^2 + n^2r^{-2})\widetilde{u}_x + (1 + \varepsilon\Gamma\eta_r s)^{-1}s^2\widetilde{u}_x + \mathrm{i}k(1 + \varepsilon\Gamma\eta_r s)^{-1}\widetilde{p}, \tag{36}$$

$$d_r \widetilde{u}_x = \widetilde{\chi}_x, \tag{37}$$

$$d_r \widetilde{\chi}_\theta = -r^{-1}\widetilde{\chi}_\theta + [r^{-2}(1 + n^2) + k^2]\widetilde{u}_\theta - 2\mathrm{i}nr^{-2}\widetilde{u}_r + (1 + \varepsilon\Gamma\eta_r s)^{-1}[s^2\widetilde{u}_\theta + \mathrm{i}nr^{-1}\widetilde{p}], \tag{38}$$

$$d_r \widetilde{u}_\theta = \widetilde{\chi}_\theta, \tag{39}$$

where the vectors $(\widetilde{\xi}_r, \widetilde{\xi}_\theta, \widetilde{\xi}_x)$ and $(\widetilde{\chi}_r, \widetilde{\chi}_\theta, \widetilde{\chi}_x)$ are, respectively, the derivative of $(\widetilde{v}_r, \widetilde{v}_\theta, \widetilde{v}_x)$ and $(\widetilde{u}_r, \widetilde{u}_\theta, \widetilde{u}_x)$ with respect to r.

6. Numerical method

The differential equations (28)–(39) and their equivalent for the axisymmetric disturbances were solved using a fourth-order Runge–Kutta method to obtain three independent solutions, $(\mathbf{X}_1, \mathbf{X}_2, \mathbf{X}_3)$, each of which satisfy the boundary conditions at $r = 1$. The components of the vectors $\mathbf{X}_i$, $i = 1, 2, 3$, are the velocity components, their first-order derivatives with respect to r, and the pressure in the fluid medium. The independence of the three solutions, $\mathbf{X}_i$, is ensured by starting the computation with one of the three independent vectors formed by several values of the vector $(\widetilde{\xi}_x, \widetilde{\xi}_\theta, \widetilde{p}_f)$ at $r = 1$. For instance, $\mathbf{X}_1$ can be obtained by starting the computation with the boundary condition

$$\mathbf{X}_1 = (\widetilde{v}_x, \widetilde{v}_r, , \widetilde{v}_\theta, \widetilde{p}_f, \widetilde{\xi}_\theta, \widetilde{\xi}_x)^{\mathrm{T}} = (0, 0, 0, 1, 0, 0)^{\mathrm{T}}, \quad r = 1;$$

$\mathbf{X}_2$ can be obtained by starting the computation with the boundary condition

$$\mathbf{X}_2 = (\widetilde{v}_x, \widetilde{v}_r, , \widetilde{v}_\theta, \widetilde{p}_f, \widetilde{\xi}_\theta, \widetilde{\xi}_x)^{\mathrm{T}} = (0, 0, 0, 0, 1, 0)^{\mathrm{T}}, \quad r = 1;$$

and $\mathbf{X}_3$ can be obtained by starting the computation with the boundary condition

$$\mathbf{X}_3 = (\widetilde{v}_x, \widetilde{v}_r, , \widetilde{v}_\theta, \widetilde{p}_f, \widetilde{\xi}_\theta, \widetilde{\xi}_x)^{\mathrm{T}} = (0, 0, 0, 0, 0, 1)^{\mathrm{T}}, \quad r = 1.$$

With this choice, the boundary conditions at $r = 1$ are satisfied by all solutions, namely $\mathbf{X}_1$, $\mathbf{X}_2$ and $\mathbf{X}_3$. It should be noted that the chosen values $(\widetilde{v}_x, \widetilde{v}_r, , \widetilde{v}_\theta, \widetilde{p}_f, \widetilde{\xi}_\theta, \widetilde{\xi}_x)^{\mathrm{T}}$ at $r = 1$ to initiate the computation of $\mathbf{X}_1$, $\mathbf{X}_2$ and $\mathbf{X}_3$ must form a set of free vectors, which is sufficient for $\mathbf{X}_1$, $\mathbf{X}_2$ and $\mathbf{X}_3$ to be free vectors. Then the general solution in the fluid medium is an arbitrary combination of the three free solutions $\mathbf{X}_1$, $\mathbf{X}_2$ and $\mathbf{X}_3$, such that

$$\mathbf{Z}_1 = A_1\mathbf{X}_1 + A_2\mathbf{X}_2 + A_3\mathbf{X}_3, \tag{40}$$

where (A_1, A_2, A_3) are arbitrary constants.

Similarly, for the displacement field in the solid, we solve for three independent solutions, $(\mathbf{Y}_1, \mathbf{Y}_2, \mathbf{Y}_3)$, each of which satisfy the boundary conditions at $r = 0$. The components of the vectors $\mathbf{Y}_i$, $i = 1, 2, 3$ are the components of the displacement vector and their first-order derivative with respect to r and the pressure in the solid medium. The independence of the solutions is ensured by beginning the computation with one of the three independent values of the vector $(\widetilde{\chi}_x, \widetilde{\chi}_\theta, \widetilde{p}_s)$ at $r = 0$. For instance, $\mathbf{Y}_1$ can be obtained by starting the computation with the boundary condition

$$\mathbf{Y}_1 = (\widetilde{u}_x, \widetilde{u}_r, , \widetilde{u}_\theta, \widetilde{p}_s, \widetilde{\chi}_\theta, \widetilde{\chi}_x)^{\mathrm{T}} = (0, 0, 0, 1, 0, 0)^{\mathrm{T}}, \quad r = 0;$$

$\mathbf{Y}_2$ can be obtained by starting the computation with the boundary condition

$$\mathbf{Y}_2 = (\widetilde{u}_x, \widetilde{u}_r, , \widetilde{u}_\theta, \widetilde{p}_s, \widetilde{\chi}_\theta, \widetilde{\chi}_x)^{\mathrm{T}} = (0, 0, 0, 0, 1, 0)^{\mathrm{T}}, \quad r = 0;$$

and $\mathbf{Y}_3$ can be obtained by starting the computation with the boundary condition

$$\mathbf{Y}_3 = (\widetilde{u}_x, \widetilde{u}_r, , \widetilde{u}_\theta, \widetilde{p}_s, \widetilde{\chi}_\theta, \widetilde{\chi}_x)^{\mathrm{T}} = (0, 0, 0, 0, 0, 1)^{\mathrm{T}}, \quad r = 0;$$

by this choice, the boundary conditions at $r = 0$ are satisfied by all solutions, namely $\mathbf{Y}_1$, $\mathbf{Y}_2$ and $\mathbf{Y}_3$. It should be noted that the chosen values $(\widetilde{u}_x, \widetilde{u}_r, , \widetilde{u}_\theta, \widetilde{p}_s, \widetilde{\chi}_\theta, \widetilde{\chi}_x)^{\mathrm{T}}$ at $r = 0$ to initiate the computation of $\mathbf{Y}_1$, $\mathbf{Y}_2$ and $\mathbf{Y}_3$ must form a set of free vectors, which is sufficient for $\mathbf{Y}_1$, $\mathbf{Y}_2$ and $\mathbf{Y}_3$ to be free vectors. Then, the general solution in the solid medium is an arbitrary combination of the three free solutions $\mathbf{Y}_1$, $\mathbf{Y}_2$ and $\mathbf{Y}_3$, such that

$$\mathbf{Z}_2 = B_1\mathbf{Y}_1 + B_2\mathbf{Y}_2 + B_3\mathbf{Y}_3, \tag{41}$$

where (B_1, B_2, B_3) are arbitrary constants. The boundary conditions at $r = 0.1$ lead to the eigenvalue problem

$$\mathbf{MC} = 0, \tag{42}$$

where the elements of the 6×6 matrix $\mathbf{M}$ are a linear combination of the particular solution components $(\mathbf{X}_1, \mathbf{X}_2, \mathbf{X}_3)$, $(\mathbf{Y}_1, \mathbf{Y}_2, \mathbf{Y}_3)$ and their derivatives with respect to r at $r = 0.1$, which involve $k, n, \mathrm{Re}, \eta_r$ and Γ. The components of the vector $\mathbf{C}$ are the six arbitrary constants A_1, A_2, A_3, B_1, B_2 and B_3. The characteristic equation is obtained by setting the determinant of the characteristic matrix $\mathbf{M}$ to zero. The solution of the characteristic equation gives the growth rate as a function of the Reynolds number for different values of the parameters k, n, η_r and Γ.

In order to find the eigenvalues of the system, one has to find the zero of the determinant D, of the matrix $\mathbf{M}$. The method used by Hamadiche and Gad-el-Hak (2002) has been used. However, this method has the disadvantage of the existence of various stable modes of low frequency and low damping rate which yields a high-order polynomial. Moreover, the modes are too close to define precisely the contour of integration and to isolate them in different domains. Therefore, we decided to sweep out the complex (amplification rate, frequency)-plane. For this task, the complex plane has been divided into a set of large number of small cells (as shown in Fig. 6). The corners of these cells

are used as initial conditions for the Newton–Raphson method to converge toward the eigenmodes. The code successfully converges all the time for the nearest eigenvalue without overflow.

7. Unstable modes

The technique described in the above section predicts more than one unstable mode, and shows that the system is unstable to nonaxisymmetric disturbances. Two categories of unstable modes were found and termed G_1 and G_2. The first category, G_1, has a small amplification rate in comparison with the amplification rate of the second category, G_2. The frequency of the category, G_1, is much lower than the frequency of the category G_2. The ratio of the amplification rates is about 40. The G_1 category concerns the flow at low and high Reynolds number. G_2 concerns only the flow having two-cell form: $\tilde{\mathrm{R}}\mathrm{e} \geqslant 1$. In the next two sections, we study in detail these two groups of unstable modes.

8. Analysis of the G_1 group

The group, G_1, contains only one unstable mode before the bifurcation of the basic flow, i.e. when the Reynolds number $\tilde{\mathrm{R}}\mathrm{e} \leqslant 0.2$. Two unstable modes have been observed after the bifurcation of the basic flow, i.e. when the Reynolds number $\tilde{\mathrm{R}}\mathrm{e} \geqslant 5$. These unstable modes are characterized by a small amplification rate when compared to the amplification rate of the second group [see Fig. 7(a)]. Moreover, this instability takes the form of a long wave (small wavenumber), while our assumption of local stability analysis limits the validity of our analysis to waves shorter than the die length (large wavenumber). In fact, the local analysis neglects the variation of the basic flow in the x direction and consequently does not take account of the boundary conditions at $x = -2$ and 2. Thus, the mode has to be short enough in order to justify neglecting the effect of the boundary conditions at $x = -2$ and 2. Furthermore, a wave having a length greater than the length of the die should not exist within the die. This short wave could be a source term, that creates a long wave, which propagates only in the optical fiber far from the die. As our analysis is related to waves that are supposed to be simultaneously in the fluid medium within the die and in the optic fiber, one has to disregard the waves having a length greater than the length of the die. For these reasons, we disregard these kinds of waves and conclude that these instabilities are not the cause of the vibration observed in the experiment.

However, Fig. 7(b) shows that the frequency decreases when the wavenumber increases, indicating a negative group velocity, $V_g = -\mathrm{d}s_r/\mathrm{d}k$. Group G_1 shows a strange behavior in which the increase in the viscosity of the optical fiber leads to an increase in the amplification rate of the unstable modes belonging to this group. This strange behavior indicates that unstable G_1 modes belong to class A instability introduced by Benjamin (1963), more often termed negative-energy waves. The frequency and the amplification rate of the unstable modes, belonging to the G_1 group, are examined when Γ goes to zero (the fiber then behaves like a rigid solid). We found that the amplification rate, as well as the frequency, reaches finite values when Γ tends to zero, indicating that these modes are flow-based modes under the classification of Carpenter and Garrad (1985, 1986).

9. Analysis of the G_2 group

The group, G_2, contains more unstable modes than the group G_1. They exist only for the flow regime corresponding to $\tilde{\mathrm{R}}\mathrm{e} \geqslant 1$ confirming the experimental observation. The amplification rates versus the frequency of this group are shown in Fig. 8, for three stations in the die located at $x = -1.34$, 0 and $+1.34$. It should be noted that at the middle station, $x = 0$, a part of the unstable modes is canceled. This may be explained by the form of the basic flow profile in the middle of the die, where the inflexion point is quasi-absent, as shown in Fig. 5. Note that the most destructive mode has a low frequency. However, Fig. 8 shows that there is a set of unstable modes with frequencies approximately equal to ± 37.5 for the same azimuthal wavenumber $n = 1$ and axial wavenumber $k = 2$. These modes form a group of resonant modes, which may form a harmful instability too, even though their amplification rates are relatively moderate, in comparison with the amplification rate of the most destructive mode.

In Fig. 9(a), we represent the amplification rates and the frequencies of the most dangerous modes versus the wavenumber. The amplification rates and the frequencies vary linearly with the wavenumber and the amplification rate remains positive for large wavenumber, as shown in Fig. 9(a). Therefore, the waves smaller than the die length are unstable, which is consistent with our assumption of local stability analysis. Note that the form of dependence between the amplification rate and frequency on the one hand and the wave number, on the other, is observed in

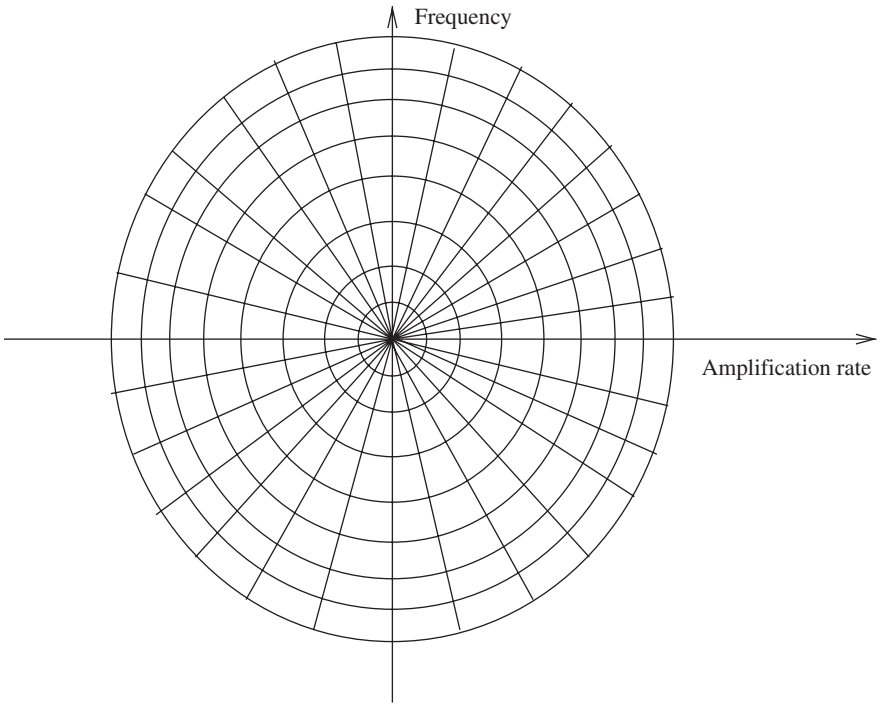

Fig. 6. The locus of the points in the complex (amplification rate, frequency)-plane used as initial condition for the search for the eigenvalues.

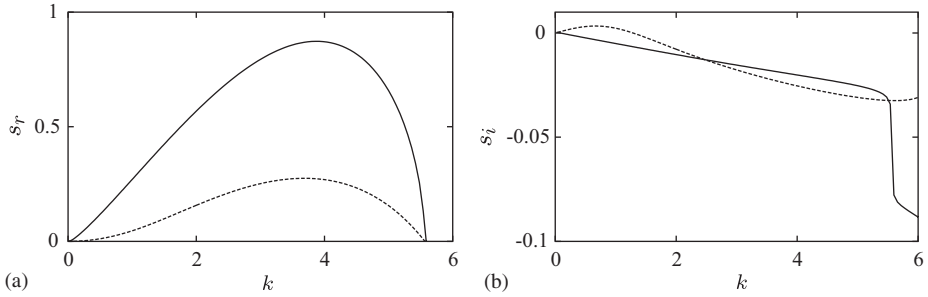

Fig. 7. (a) The amplification rate versus the wave number of the weakly unstable mode, group G_1. (b) The frequency of weakly unstable modes versus the wave number, group G_1. —, $\tilde{\mathrm{Re}} = 5$; - - -, $\tilde{\mathrm{Re}} = 0.1$. $\Gamma = 0.02$, $\eta_r = 0$, the azimuthal wavenumber $n = 1$.

the Kelvin–Helmholtz instability in a shear layer [see Drazin and Reid (1995, p. 14–23)]. Indeed, our basic flow has, in some region of the die, an opposite flow and an inflection point, which leads to a similar Kelvin–Helmholtz instability.

It is found that the viscosity of the optical fiber has an insignificant effect on these modes, indicating again that these instabilities are a Kelvin–Helmholtz type. Owing to the effect of viscosity on these modes, one can classify them as belonging to class C in the Benjamin (1963) classification.

In order to classify these modes using the method introduced by Carpenter and Garrad (1985), we have examined the limit of the amplification rate and the frequency when Γ tends to zero, i.e. when the optical fiber behaves like a rigid wall. It was found that the amplification rate and the frequency tend to zero when Γ approaches zero. This result indicates that these modes exist for the case of a quasi-rigid wall, but with a very low amplification rate. This means that their origin is in the fluid, and that they are fluid-based modes. However, they are greatly amplified by the elasticity of the optical-fiber structure.

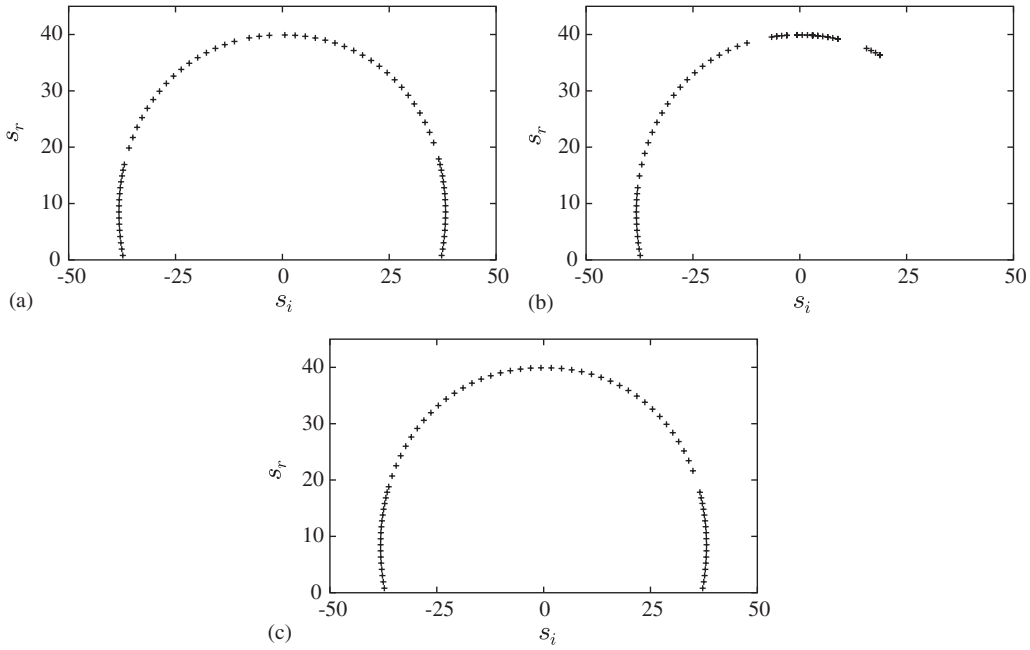

Fig. 8. Amplification rate versus the frequency of the unstable modes, group G_2, at the following three stations: (a) station number one, $x = -1.34$, (b) station number two, $x = 0$, (c) station number three, $x = 1.34$. $\mathrm{Re} = 50$, $\tilde{\mathrm{Re}} = 5$, $\Gamma = 0.02$, $\eta_r = 0$, the azimuthal wavenumber $n = 1$, the axial wavenumber $k = 2$.

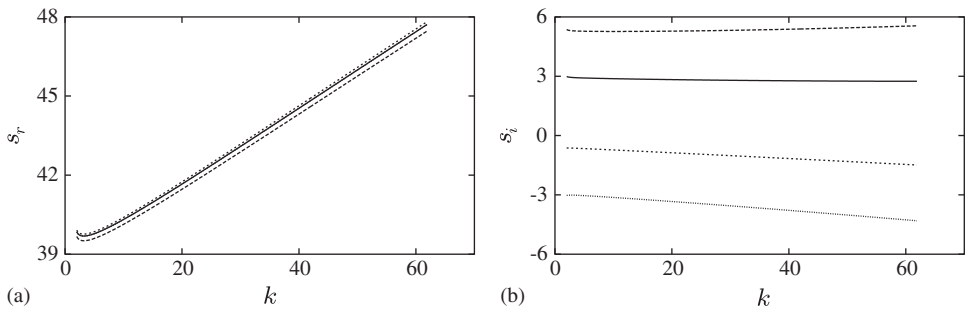

Fig. 9. (a) Amplification rates of the most unstable modes versus the wavenumber k, group G_2, at the first station $x = -1.34$. (b) The frequencies of the most unstable modes versus the wavenumber k, group G_2, at the first station, $x = -1.34$. $\mathrm{Re} = 50$, $\tilde{\mathrm{Re}} = 5$, $\Gamma = 0.02$, $\eta_r = 0$, the azimuthal wavenumber $n = 1$.

It is found that the frequencies of the unstable modes change slightly with the variation of the wave number, as shown in Fig. 9(b). The form of the curves, shown in Fig. 9(b), indicates that the group velocity of these modes may be positive, negative or zero, depending on the sign and the value of the function, $\partial s_i/\partial k$. Furthermore, the group velocity of those unstable modes is very small in comparison with the speed of the optical fiber. It is well known that the absolute instability is a notion related only to open systems (Briggs, 1964). However, the analysis we made here is valid for the short-wave modes (large wavenumber). Therefore, the length of the unstable wave is small in comparison with the die length. Thus, the local analysis is equivalent to the analysis of an open system. Therefore, in the limit of our assumption, one can examine the instability to see if it is absolute or convective. The fact that the group velocity of the unstable mode is very low may indicate a high probability for the existence of absolute instabilities, which could be the subject of a future study.

As mentioned above, the G_2 group does not exist at low Reynolds number, e.g. $\tilde{\mathrm{Re}} \leqslant 0.2$, where the basic flow takes a one-cell form. Moreover, it exists only when the basic flow bifurcates to a two-cell form, i.e. $\tilde{\mathrm{Re}} \geqslant 1$, although the basic

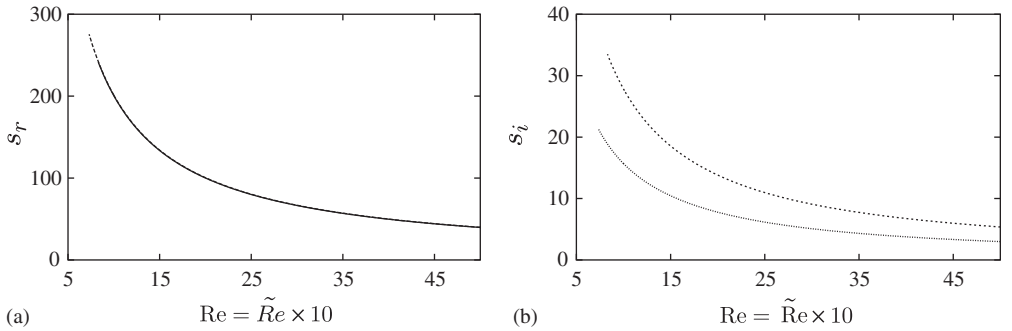

Fig. 10. The amplification rate and frequency versus the Reynolds number of two unstable modes at the first station, $x = -1.34$. The axial wavenumber $k = 2$, $\Gamma = 0.02$, $\eta_r = 0$, the azimuthal wavenumber $n = 1$.

flow seems to bifurcate smoothly when the Reynolds number increases. In order to examine the behavior of the G_2 group, as the Reynolds number approaches the critical value from above, we present in Fig. 10 the amplification rate and frequency versus the Reynolds number. At each Reynolds number value in the graph, the basic flow has been computed. Fig. 10(a) suggests that the amplification rate diverges when the Reynolds number tends toward the value at which the basic flow bifurcates. Fig. 10(b) suggests that the frequency diverges as well at this critical Reynolds number value. It was impossible to follow the computation in order to reduce the Reynolds number below this value. This indicates that those modes are in fact related to the flow regime where $\widetilde{\mathrm{Re}} \geqslant 1$.

The fact that the modes diverge to leave the system, when some of its control parameters vary, is observed in other circumstances. For instance, in swirling flow, Hamadiche and Atassi (2003) observed that the most propagated acoustic modes formed by the coalescence of two acoustic modes is cut off when the Mach number reaches some critical value. The cut off is accompanied by the divergence of the frequency of the acoustic wave. This phenomenon is not physical, because the frequency has a finite value. This mode behavior corresponds to the fact that the basic flow is forced to be steady for the control parameters under consideration, whereas, in fact, it has to be an unsteady one (private communication from Atassi). Note that, similar unstable modes have been obtained for the azimuthal wavenumber $1 < n \leqslant 6$. There is no significant variation of the amplification rates or frequencies of the unstable modes in this range of azimuthal wave number.

10. Surface tension effects on the coat deformation

We consider the effects of gravity and surface tension on a film of resin in its liquid phase, at the die outlet. We suppose that the film is axisymmetric, with radius R, and that it has a circular cross-section. The axis of the film is parallel to the gravity field which itself is parallel to the axes of the optical fiber (see Fig. 3). We suppose that the radius of the optical fiber and the thickness of the film are small enough to allow the surface tension to be the dominant force in the flow under consideration. Let R_1 and R_2 be the two principal radii of the surface of the film. Then the pressure jump on the surface is

$$\Delta p = \gamma \left(\frac{1}{R_1} + \frac{1}{R_2} \right). \tag{43}$$

Due to the fact that the flow is axisymmetric, the film-surface equation, in cylindrical coordinates described in Fig. 3, reads

$$r = R(x). \tag{44}$$

The normal to the surface is

$$\mathbf{n} = \frac{(1, 0, -R')}{(R'^2 + 1)^{1/2}}. \tag{45}$$

Considering the atmospheric pressure as the origin of the pressure, the force on the surface of the film due to surface tension is

$$\mathbf{F} = -\int_s \mathbf{n} p \, \mathrm{d}s = -\int_s (n_x \mathbf{x} + n_r \mathbf{e_r}) p \, \mathrm{d}s = \mathbf{x} \int_s p \frac{R'}{(R'^2 + 1)^{1/2}} \, \mathrm{d}s; \tag{46}$$

the term containing $\mathbf{e_r}$ is eliminated owing to the axial symmetry.

10.1. Principal curvature radii

In order to compute the pressure jump due to the surface tension, we need the principal radii of curvature. Due to the symmetry of the problem, one of the principal radii, we name R_1, is equal to the cross-section radius $R+R_0$. We consider in our analysis the case where $R_0 \ll R_c$, so that $R_1 \approx R$. The other principal radius has to be computed as follows. The equation of the surface is invariant under rotation around the x-axis, so the equation of the surface is any function $R=R(x)$ that reveals the variation of the radius with axial distance in the (x,r)-plane. The slope of the curve in the (x,r)-plane is

$$\tan(\theta)=\frac{\mathrm{d}R(x)}{\mathrm{d}x}=R'; \tag{47}$$

the angle θ is the angle formed by the tangent to the curve and the x-axis. From the foregoing equation one can write

$$d(\tan(\theta))=(1+\tan^2(\theta))\,\mathrm{d}\theta=R''\,\mathrm{d}x, \tag{48}$$

so

$$\frac{\mathrm{d}\theta}{\mathrm{d}x}=\frac{R''}{1+\tan^2(\theta)}=\frac{R''}{1+R'^2}; \tag{49}$$

the curvature radius R_1 is defined by

$$R_1\,\mathrm{d}\theta=\mathrm{d}c=(\mathrm{d}x^2+\mathrm{d}R^2)^{1/2}=\mathrm{d}x(1+R'^2)^{1/2} \tag{50}$$

which leads to

$$\frac{1}{R_1}=\frac{\mathrm{d}\theta}{\mathrm{d}x}\frac{1}{(1+R'^2)^{1/2}}=\frac{R''}{(1+R'^2)^{3/2}}. \tag{51}$$

The pressure jump is

$$p=\gamma\left(\frac{1}{R}+\frac{R''}{(1+R'^2)^{3/2}}\right), \tag{52}$$

γ being a constant depending on the material propriety. Using Eq. (52) and the fact that

$$\mathrm{d}s=2\pi R\,\mathrm{d}c=2\pi R[(\mathrm{d}x)^2+(\mathrm{d}R)^2]^{1/2}=2\pi R(1+R'^2)^{1/2}\,\mathrm{d}x$$

and performing the integration over the surface limited by x and $x+\mathrm{d}x$, Eq. (46) reads

$$\mathbf{F}=2\pi\gamma\mathbf{x}\int_x^{x+\mathrm{d}x}\left(R'+\frac{RR'R''}{(1+R'^2)^{3/2}}\right)\mathrm{d}x=2\pi\gamma\mathbf{x}\left(R'+\frac{RR'R''}{(1+R'^2)^{3/2}}\right)\mathrm{d}x=2\pi RR'p\,\mathrm{d}x\,\mathbf{x}, \tag{53}$$

$$\mathbf{F}=2\pi RR'p\,\mathrm{d}x\,\mathbf{x}, \tag{54}$$

where $\mathrm{d}x$ is an infinitesimal increment.

10.2. Equilibrium equation

As the film is thin in comparison with the radius of the optical fiber, we suppose that the pressure does not vary over the section, and that it depends only on the axial distance. The momentum balance applied to the volume element, indicated in Fig. 3, leads to the equilibrium equation

$$(\pi(R^2p)_x-\pi(R^2p)_{x+\mathrm{d}x})\mathbf{x}+\mathbf{F}-\rho g\pi R^2\,\mathrm{d}x\,\mathbf{x}=\rho\int_s\mathbf{v}\mathbf{v}.\mathbf{n}\,\mathrm{d}s=\rho((u^2s)_x-(u^2s)_{x+\mathrm{d}x})\mathbf{x}, \tag{55}$$

$$-\frac{\mathrm{d}(R^2p)}{\mathrm{d}x}+2RR'p-\rho gR^2=-\rho\frac{\mathrm{d}(u^2R^2)}{\mathrm{d}x}. \tag{56}$$

The conservation of mass gives

$$u=u_0\left(\frac{R_c}{R}\right)^2, \tag{57}$$

so Eq. (56) becomes

$$-\frac{\mathrm{d}(R^2p)}{\mathrm{d}x}+2RR'p-\rho gR^2=-R_c^4u_0^2\rho\,\frac{\mathrm{d}(R^{-2})}{\mathrm{d}x}. \tag{58}$$

The dynamic equations are

$$\frac{1}{R}+\frac{R''}{(1+R'^2)^{3/2}}-\frac{p}{\gamma}=0, \tag{59}$$

$$-\frac{\mathrm{d}(R^2p)}{\mathrm{d}x}+2RR'p-\rho gR^2-2R_c^4u_0^2\rho\,\frac{R'}{R^3}=0, \tag{60}$$

or equivalently

$$\frac{R''}{(1+R'^2)^{3/2}}+\frac{1}{R}-\frac{p}{\gamma}=0, \tag{61}$$

$$\frac{(\mathrm{d}p)}{\mathrm{d}x}+\rho g+2R_c^4u_0^2\rho\,\frac{R'}{R^5}=0. \tag{62}$$

10.3. Dimensionless equations

In order to obtain dimensionless equations, we scale the distance by the inlet diameter, R_c, and the pressure by γR_c^{-1}, γ being the coefficient of the surface tension. We define the dimensionless pressure $\pi=R_cp\gamma^{-1}$, and $Y=RR_c^{-1}$, $X=xR_c^{-1}$ the dimensionless radial and axial distance, respectively. The dynamic equations then become

$$\frac{Y''}{(1+Y'^2)^{3/2}}+\frac{1}{Y}-\pi=0, \tag{63}$$

$$\frac{(\mathrm{d}\pi)}{\mathrm{d}X}+H_1+H_2\,\frac{Y'}{Y^5}=0, \tag{64}$$

$$H_1=\frac{\rho gR_c^2}{\gamma},\quad H_2=\frac{2\rho R_cu_0^2}{\gamma}. \tag{65}$$

The dimensionless number H_1 is the ratio of the gravity and the surface tension forces, and H_2 is the ratio of the inertia and the surface tension forces.

10.4. Numerical solution

In order to solve the system of equations given above by the Runge–Kutta method we write it in the form

$$\frac{\mathrm{d}Y}{\mathrm{d}X}=\psi, \tag{66}$$

$$\frac{\mathrm{d}\psi}{\mathrm{d}X}=-\frac{1}{Y}(1+\psi^2)^{3/2}+\pi(1+\psi^2)^{3/2}, \tag{67}$$

$$\frac{(\mathrm{d}\pi)}{\mathrm{d}X}=-H_1-H_2\,\frac{\psi}{Y^5}. \tag{68}$$

Figs. 11 and 12 show the wavy form of the coating surface, described by Eqs. (66)–(68). The system of differential equations, (66)–(68), involve two dimensionless parameters, namely H_1 and H_2. H_1 is the ratio of the gravity and surface-tension forces; H_2 is the ratio of inertia and surface tension-forces. The proposed model predicts a wavy form for the optical fiber surface coating. Fig. 11 shows that the surface of the fiber has a wavy form. Fig. 12 shows that the length of the wave depends on the two parameters H_1 and H_2. Furthermore, Fig. 12 shows that the maximum wavelength is of the order of magnitude of the radius of the fiber. For a fixed H_2, it is found that the wavelength decreases with increasing H_1 and reaches its maximum value for $H_1=0$. When $H_1=H_2$ the surface oscillation becomes very sharp, leading to a breakdown of the optical-fiber coating, as depicted in Fig. 12. Furthermore, increasing

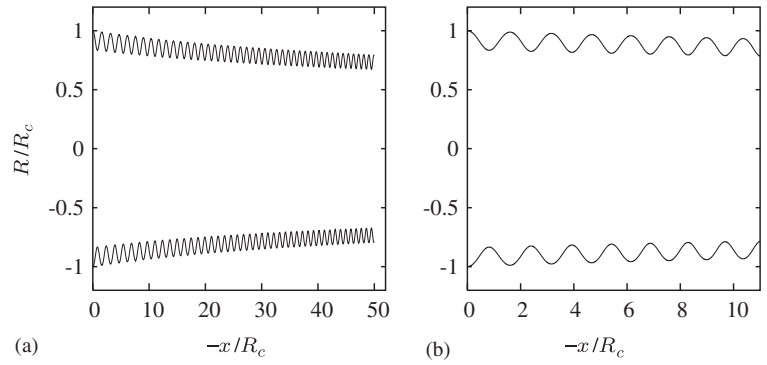

Fig. 11. Oscillation of the fiber cable surface during the coating process; (b) is an enlargement of the first part of (a). $H_1 = 0.1$, $H_2 = 10$.

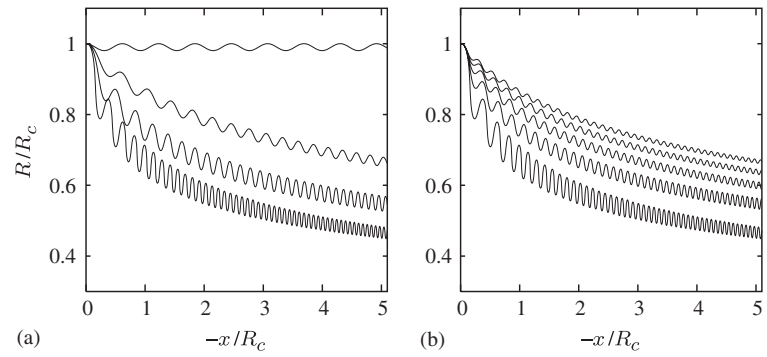

Fig. 12. Oscillation of the fiber cable surface during the coating process. (a) $H_2 = 100$ and, from above, $H_1 = 0$, $H_1 = 20$, $H_1 = 50$, $H_1 = 100$. (b) $H_1 = 100$, and, from below, $H_2 = 100$, $H_2 = 200$, $H_2 = 300$, $H_2 = 400$, $H_2 = 500$.

H_1 leads to decreases in the thickness of the optical-fiber coating, causing the coating to break. For fixed H_1, the amplitude of the wave decreases with increasing H_2. For low values of H_2, the amplitude of the wave may reach half of the fiber radius.

11. Conclusions

In the present work, we consider the stability of the optical-fiber coating system. In the first stage, the optical fiber is assumed to be a rigid solid, propelled at constant speed, and passing through a die, which is filled by a resin. The die is supplied by the resin through a slit in the top that leaves the die through a slit around the optical fiber. The two-dimensional Navier–Stokes equations, associated with the appropriate boundary conditions in (ψ, ω) formulation, are solved to find the behavior of the resin in the die.

It has been found that, for Reynolds number less than the experimental critical Reynolds number estimated by Kaneko et al. (2002), the basic flow exhibits a one-cell pattern. For a Reynolds number higher than the experimental critical Reynolds number given by Kaneko et al. (2002), the basic flow consists of two-cell patterns. In the later case the basic flow has an inflection point.

In the second stage, we have considered the optical fiber as a viscoelastic medium interacting with the previously computed basic flow in the die. The stability of the system composed of the optical fiber considered as a viscoelastic medium and the basic flow has been studied. Both axisymmetric and nonaxisymmetric disturbances were considered. It was found that the system is unstable to nonaxisymmetric disturbances. Moreover, there are two groups of unstable modes, termed G_1 and G_2.

The group G_1 represents an instability having a small wavenumber, which is not compatible with the local-stability-analysis hypothesis that we have made. Therefore, this instability is not the origin of the vibration observed in the experiment of Kaneko et al. (2002). However, the analysis of the unstable modes of this group leads to the conclusion that they are fluid-based modes, which belong to class A in the Benjamin classification. Note that these modes exist for low- and high-Reynolds number flow regimes and only for the azimuthal wave number $n = 1$. Moreover, at low Reynolds number, only one mode has been found having a relatively small amplification rate; at high Reynolds number only two modes have been found having a relatively small amplification rate.

The group G_2 is a short-wave instability compatible with our local-stability-analysis hypothesis. The most unstable mode is one of relatively low frequency. The group G_2 has a large number of unstable modes covering a broad frequency range, and they exist for the azimuthal wavenumber $n \geqslant 1$. Among the unstable modes, there is a set of unstable modes having the same frequency and the same wavenumber, leading to the resonance of the system. The group G_2 does not exist when the Reynolds number is under the experimental critical value. The elasticity of the optical fiber leads to a dramatic increase in the amplification rate of these modes. Based upon the importance of the amplification rate, the resonance and the large number of the unstable modes in this group, we have concluded that this group is the cause of the optical-fiber vibration observed in the experiment.

A model based on the surface-tension forces is proposed to explain a possible irregularity of the coating surface. In this model, the resin at the outlet of the die is assumed to be in its liquid phase. The formulation of the problem leads to the third-order nonlinear differential equation describing the coating surface. It is found that the dynamic equation depends on two dimensionless parameters, namely H_1 and H_2. H_1 is the ratio of the gravity and surface-tension forces, and H_2 is the ratio of inertia and surface-tension forces. The proposed model predicts a wavy form of the optical-fiber surface coating. The wavelength and amplitude depend on the dimensionless parameters H_1 and H_2. It has been found that the surface coating may be broken for some values of H_2 and H_1.

References

Al-Farkh, M., 1998. Stabilité des écoulements dans un divergent en rotation. Thèse présentée devant L'université Claude Bernard-Lyon 1, France.

Batchelor, G.K., 1967. An Introduction to Fluid Dynamics. Cambridge University Press, Cambridge.

Benjamin, T.B., 1963. The threefold classification of unstable disturbances in flexible surfaces bounding inviscid flows. Journal of Fluid Mechanics 16, 436–450.

Briggs, R.J., 1964. Electron-Stream Interaction with Plasmas. MIT Press, Cambridge, MA.

Carpenter, P.W., Garrad, A.D., 1985. The hydrodynamic stability of flow over Kramer-type compliant surfaces. Part 1. Tollmien-Schlichting instabilities. Journal of Fluid Mechanics 155, 465–510.

Carpenter, P.W., Garrad, A.D., 1986. The hydrodynamic stability of flow over Kramer-type compliant surfaces. Part 2. Flow-induced surface instabilities. Journal of Fluid Mechanics 170, 199–232.

Drazin, P.G., Reid, W.H., 1995. Hydrodynamic Stability. Cambridge University Press, Cambridge.

Gad-el-Hak, M., 1999. The Fluid Mechanics of Microdevices. The Freeman Scholar Lecture. ASME Journal of Fluids Engineering 121, 5–33.

Hamadiche, M., Atassi, M.H., 2003. Gust radiations. Ninth AIAA/CEAS Aeroacoustics Conference and Exhibit, Hilton Head, South Carolina, USA.

Hamadiche, M., Gad-el-Hak, M., 2002. Temporal stability of flow through viscoelastic tubes. Journal of Fluids and Structures 16, 331–359.

Hirsch, C., 1997. Numerical Computation of Internal and External Flows, vol. 1. Wiley, New York.

Inada, F., Hayama, S., 1990a. A study of leakage-flow-induced vibration, Part 1: Fluid-dynamic forces and moments acting on the walls of narrow tapered passage. Journal of Fluids and Structures 4, 395–412.

Inada, F., Hayama, S., 1990b. A study of leakage-flow-induced vibration, Part 2: Stability analysis and experiments for two-degree-of-freedom systems combining translational and rotational motions. Journal of Fluids and Structures 4, 413–428.

Kaneko, S., Yuichi, O., Tatsuo, W., 2002. Optical fiber cable vibration induced by leakage flow during coating process. Proceeding of the Fifth International Symposium on FSI, AE & FIV + N. ASME International Mechanical Engineering Congress, 17–22 November 2002, New Orleans, LA, USA.

Landau, L.D., Lifshitz, E.M., 1970. Theory of Elasticity (translated from the Russian), second ed. Pergamon Press, Oxford.

Tajima, K., 1970. Vibration Engineering, Sangyo Tosho, Tokyo, pp. 290–294 (in Japanese).

Further Reading

Thomas, L.H., 1953. The stability of plane Poiseuille flow. Physical Review 91, 780–783.